Contrail Formation Criterion for Assessment of Alternative Propulsion Technologies

Edward S. Richardson*
Faculty of Engineering and Physical Sciences, University of Southampton, Southampton, SO17 1BJ, United Kingdom

Contrail emission is the greatest non-CO_2 contribution to global climate change from aviation. This study provides a consistent methodology for comparing the contrail propensity of alternative propulsion technologies, applicable to more-electric gas turbine systems, fuel cell systems with and without external cooling, and piston engines. The method accounts for distributed propulsion and boundary layer ingestion, and for alternative fuels such as liquid hydrogen. The Schmidt-Appleman theory for contrail formation is applied rigorously without invoking the perfect gas approximation. It is found that conventional use of the perfect gas approximation, neglect of fuel mass, and neglect of the latent heat of liquid fuels results in significant errors that are easily avoided with the new method. The analysis confirms that several propulsion developments intended to reduce CO_2 emission promote contrail formation: use of hydrogen fuel, introduction of efficient fuel cell power systems (especially low-temperature fuel cell technologies), and generation and distribution of electrical power all tend to increase condensation. Boundary layer ingestion however has the opposite effect, increasing the ceiling for contrail formation by several hundred meters in the present analysis, potentially providing a practical means to reduce climate impact by decreasing both fuel consumption and contrail formation.

*Corresponding author: Professor of Applied Thermodynamics, Department of Aeronautics and Astronautics, e.s.richardson@soton.ac.uk.

Nomenclature

A	=	Area [m^2]
a,b,c,d	=	Stoichiometric coefficients
$F_{N,eff}$	=	Effective net thrust [N]
f	=	Gravimetric fuel-air ratio
G	=	Contrail parameter, dp_{H2O}/dT [$Pa.K^{-1}$]
H_{min}	=	Contrail ceiling [m]
h	=	Specific enthalpy [$J.kg^{-1}$]
p	=	Pressure [Pa]
Q_f	=	Lower calorific value [$J.kg^{-1}$]
q	=	Specific heat flux output [$J.kg^{-1}$]
T	=	Temperature [K]
V	=	Velocity [$m.s^{-1}$]
w	=	Molar mass [$kg.kmol^{-1}$]
w_x	=	Specific shaft or electrical work output [$J.kg^{-1}$]
w_b	=	Specific electrical work output from batteries [$J.kg^{-1}$]
X	=	Mole fraction
Y	=	Mass fraction
x,y,z	=	Molar ratios
α	=	Power export parameter
β	=	Heat rejection parameter
γ_i	=	Inflow velocity parameter
γ_j	=	Jet velocity parameter
δ	=	Battery power output parameter
ε	=	Ratio of molar mass of water and dry air
η_x	=	Mechanical or electrical efficiency
η_f	=	Fuel efficiency
η_p	=	Propeller efficiency
η_{tr}	=	Transfer efficiency
ϕ	=	Equivalence ratio

ρ = Density

ξ = Exhaust mixture fraction

ψ = Relative humidity

Subscripts

a = Property of air

f = Property of the fuel

i = Property of the inflow

j = Property of the exhaust

l = Property of liquid phase

s = Property of solid phase

∞ = Property of ambient fluid

mix = Property on the mixing curve

st = Stoichiometric

Superscripts

* = Saturation property

$\ominus$ = Reference conditions (298.15 K, 1 bar)

I. Introduction

Condensation trails [1] or *contrails* [2] arise when humid aircraft exhaust mixes with cold ambient air. Contrails may disperse into persistent cirrus cloud that shift the radiative balance of the atmosphere, resulting in net global warming [3]. The magnitude of the contrail cirrus heating effect is uncertain but potentially is greater than the current global warming contribution of all aeronautical carbon dioxide emissions to date [3]. Aeronautical contributions to global climate change in the form of carbon dioxide emissions may be reduced by transition to low net CO_2 fuels, including hydrogen and sustainable aviation fuels, but oxidation of these fuels still produces water vapor with the potential for contrail cirrus formation. As aviation decarbonizes, contrail cirrus is set to become the most significant climate issue for aerospace.

Contrails form only under specific atmospheric conditions, and only contrails containing ice crystals are persistent and climatically relevant. Understanding and prediction of conditions where persistent contrails might form is needed to inform operational [4, 5, 6] and technical [7, 8] measures to reduce contrail emission. Analysis of the thermodynamic conditions under which contrails form by Schmidt [9] and Appleman [2] led to formulation of simple criteria that have been applied usefully to assess contrail propensity of conventional piston- and gas turbine-engined aircraft (e.g. see Ref. [10]).

As the aircraft exhaust mixes with ambient fluid, its thermodynamic state follows a mixing curve. A necessary condition for contrail formation, referred to as the Schmidt-Appleman criterion, is for the mixing curve to pass through water-supersaturated conditions permitting condensation of liquid water droplets. For the contrail to persist, it is then necessary for the condensate to freeze.

For temperatures below the freezing point of water, it is generally assumed that condensation starts to form supercooled water droplets initially, not ice crystals, due to the rarity of ice nuclei [11, 12] as summarized by Schumann [10]. If the water droplets are sufficiently sub-cooled they may freeze to form ice particles. A temperature colder than the homogeneous freezing temperature (234 K) is typically required for small water droplets to freeze spontaneously [13], with the freezing temperature modified slightly by the presence of solutes [14]. Since sub-cooled droplets condense only at ice-supersaturated conditions (see Fig. 1), ice particles then persist until they experience conditions unsaturated with respect to ice [15].

The radiative forcing contributed by the contrail cirrus depends on the size and morphology distributions of the ice particles, both of which are affected initially by the availability of condensation nuclei [16]. Soot and ultrafine volatile particles emitted from hydrocarbon combustion engines serve as very effective and plentiful condensation nuclei so that, for conditions meeting the Schmidt-Appleman criterion that are sufficiently cold for condensate to freeze (<234 K), the number of ice particles formed tends to approach the number of particles emitted [14], [17]. For hydrogen-fuelled aircraft, in the absence of soot and ultrafine volatile aerosol emissions, liquid droplets may still nucleate on ambient aerosol particles [11], however the lower activation of the ambient nuclei leads the number of ice crystals formed to depend on the extent of sub-cooling [16] and the degree of sub-cooling depends on the shape of the mixing curve. For turbojet and turbofan engines, the mixing curve has been modeled previously as a straight line in H_2O partial pressure–temperature space with gradient, or *contrail factor*, given by (see e.g. Refs. [10, 18]

$$G = \frac{dp_{H_2O}}{dT} = \frac{c_p p_{atm}}{\epsilon} \frac{EI_{H_2O}}{(1-\eta_o)Q_f}. \quad (1)$$

The possibility of contrail formation is then assessed by extension of the mixing line, with gradient G, from the ambient conditions, as illustrated in Fig. 1. The contrail factor accounts for the effect of atmospheric conditions (pressure p_{atm}), fuel type (lower calorific value Q_f and emission index of water for each unit mass of fuel, EI_{H_2O}), and overall efficiency of the propulsion system η_o. Schumann demonstrates that the overall efficiency (ratio of propulsive work to calorific contribution of fuel) is the correct efficiency metric to use in the contrail criterion to properly account for the effect of jet kinetic energy [10]. ϵ = 0.622 is the ratio of the molar masses of water and dry air, and c_p is a representative isobaric specific heat capacity

(e.g. for cold air). The contrail factor given by Eq. (1) is formulated for the case where all of the energy derived from burning the fuel is contained within the exhaust plume (as it is for most conventional gas turbine-powered aircraft). Appleman [2] notes that analysis requires modification to account for water-cooled piston engines where radiators dissipate heat outside of the humid exhaust stream; similar modifications are also needed to account for externally-cooled low-temperature fuel cells. The modelling should also account for any water ingested from the atmosphere [19].

The threshold for onset of contrail formation corresponds to a critical mixing curve that glances the water saturation curve, as illustrated in Fig. 1. The highest ambient temperature at which condensation can occur is at the point where the critical mixing curve is tangential to the water saturation curve. This saturation temperature is referred to in the literature variously as T_{crit} or T_{max} [18]. Significant quantities of exhaust condensation only occur at lower ambient temperatures that provide a degree of sub-cooling relative to the critical mixing curve. The criterion $T_\infty < T_{max}$ therefore determines where it becomes relevant to consider contrail formation, and further analysis is then required to assess the quantity, persistence and likely radiative forcing of the condensate over its lifetime. A lower reference temperature T_{min} shown in Fig. 1 is also commonly reported, defined as the temperature above which condensation is not possible in dry air [10].

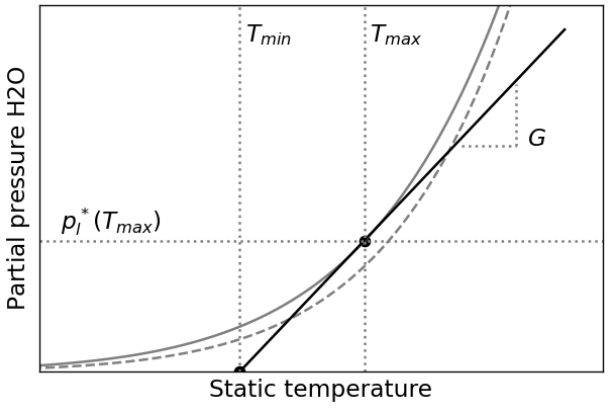

Fig. 1 Mixing curve (solid black line) in a dry atmosphere at temperature T_{min}. Ice saturation curve (dashed grey line) and liquid water saturation curve (solid grey).

Strictly, due to conservation of energy, mass and momentum during mixing, and the variation of thermodynamic properties with composition and temperature, the mixing curve is not a straight line through H_2O partial pressure-temperature space. Errors due to the common straight-line approximation have not been assessed previously to the author's knowledge, although it has been argued that the non-linear contribution of momentum mixing tends to be small for turbofan engines [10].

The type of propulsion system and the type of fuel used affect the trajectory of the mixing curve, and contrail criteria need to account for these factors. For example, Gierens showed that replacing kerosene-fuelled turbofan engines with hydrogen fuel cells substantially increases the propensity to form contrails on account of the higher water emissions index of hydrogen

fuel and also the higher efficiency of the fuel cell, which reduces the exhaust temperature [18]. While hydrogen fuel cells are likely to generate a relatively large quantity of condensate, it is argued that any contrails that form are likely to have little climate impact due to hydrogen fuel cell aircraft being envisaged for relatively low and warm altitudes, and the absence of soot emissions allowing for fewer larger droplets that settle relatively quickly.

Gierens' analysis applies to uncooled fuel cells, which yield exhaust temperatures around 500-1000°C. These high operating temperatures are feasible for Solid Oxide type fuel cells [20] but not for Proton Exchange Membrane (PEM) fuel cells that are limited currently to less than 100°C, or prospectively up to 200°C in so-called high-temperature PEM fuel cells [21]. The exhaust temperature typically is close to the fuel cell operating temperature, and external cooling of PEM fuel cells resultsi in disproportionately cold and humid exhaust that is prone to generating condensation. The previous analysis requires further development in order to account for the substantial cooling and reduced exhaust temperature of PEM systems.

A wide range of propulsion architectures are currently under evaluation for future aircraft, in addition to fuel cells, and there remains a need for systematic analysis of their impact on contrail formation. It is necessary to consider piston engines, gas turbines and all types of fuel cells, as well as the impact of battery electric storage [22]. It is necessary also to assess the impact of a move towards distributed propulsion [23], towards 'more electric aircraft' [24], and effects of using boundary layer ingestion to improve propulsive performance (e.g. see Ref. [25]).

This study develops a generalized model for the exhaust properties from a wide range of future propulsion systems and fuels. The effects of different propulsion architectures on contrail formation are then illustrated by evaluating the Schmidt-Appleman criterion rigorously, enforcing conservation of mass and energy, and accounting for the variation of thermodynamic properties with composition and temperature.

II. Formulation

The potential for contrail formation is assessed by generalized modeling of the humidity and enthalpy of the exhaust for alternative propulsion systems (subsection A), calculating the mixing curve describing the thermodynamic states arising during mixing of the exhaust with the atmosphere (subsection B), and comparing the mixing curve and the liquid water and ice-saturation curves (subsection C). For comparison with previous work, a generalized perfect gas model is also developed (subsection D).

A. Generalized exhaust model

Assessment of contrail formation relies on a model for the humidity and stagnation enthalpy of the exhaust flow. A propulsion system may issue several separate propulsive streams. For example, a turbofan engine issues a hot/humid core flow surrounded by a cold/dry bypass flow. If the separate streams mix within a short distance from the aircraft, as is the case

for a turbofan engine, the separate streams are commonly considered as one combined stream for the purposes of contrail assessment. The same combined approach is commonly adopted when assessing the propeller wash and engine exhaust of piston-engined propeller-driven aircraft, provided that the engine exhaust and any cooling air flows are discharged within and mixed into the propeller wash [2]. However, the same approach is not appropriate for a range of propulsion architectures now under consideration, especially for turboelectric and fuel-cell aircraft, where the power unit and the electric propulsors are not necessarily co-located. Instead, it is necessary to model the humidity and enthalpy of each of the aircraft's exhaust streams that remain separate. Here we propose a model for the composition and enthalpy of an individual exhaust stream, applicable to all sorts of exhaust streams within a propulsion systems, as illustrated in Fig. 2.

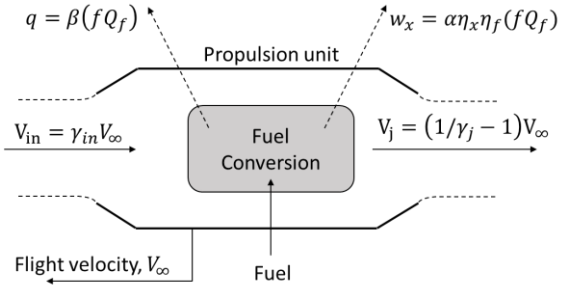

Fig. 2 Schematic of the generalized propulsion unit, with inflow velocity V_{in}, outflow velocity V_j, specific heat output q, specific power output w_x.

The model assumes steady-state flight at speed V_∞. The power unit ingests air with velocity V_{in}, which may differ from the flight speed due to installation effects, for example due to boundary layer ingestion. In this work the inlet air velocity is related to the flight velocity using an inlet velocity parameter,

$$\gamma_i = \frac{V_{in}}{V_\infty}. \tag{2}$$

The gravimetric fuel-air-ratio is f and the lower calorific value of the fuel is Q_f. For each unit mass of air flow, the chemical energy of the fuel fQ_f is converted to potential work [26] with fuel efficiency η_f. A fraction α of the potential work is converted with mechanical/electrical efficiency η_x into shaft work and/or electrical power w_x that is exported from the propulsion unit,

$$w_x = \alpha\eta_x\eta_f fQ_f. \tag{3}$$

It has been assumed here that any heat dissipated in mechanical or electrical energy conversion is absorbed into the humid exhaust stream.

The remaining fraction of the potential work accelerates the flow through the propulsion unit, converting work potential into kinetic energy of the propulsive flow with transfer efficiency η_{tr} [27],

$$\frac{1}{2}\left[(1+f)V_j^2 - V_{in}^2\right] = (1-\alpha)\eta_{tr}\eta_f f Q_f. \tag{4}$$

The jet velocity V_j depends on the engine type and its operation. In this work the jet velocities of different engines are related to the flight velocity using a jet velocity parameter,

$$\gamma_j = \frac{2V_\infty}{V_\infty + V_j}. \tag{5}$$

Where engines are installed in the free-stream (e.g. on pylons below the wing) such that $V_{in} = V_\infty$, the jet velocity parameter can be understood as a propulsive efficiency [27]. In the limit where jet velocity is equal to zero (e.g. for some on-board power generators), $\gamma_j = 2$.

The specific work w_x exported from the propulsion unit may be used to drive other propulsors with separate exhaust flows, for example in a distributed electrical propulsion system. The specific work can also take a negative value ($\alpha < 0$) if an external power source, such as a battery pack, provides a net work input to the propulsion unit in question.

Certain kinds of propulsion unit, such as piston engines and PEM fuel cell units, require cooling. If the cooling system transfers heat outside of the propulsive flow, an external heat flow arises, denoted q in Fig. 2. The quantity of heat transferred out of the propulsive flow is characterized in this work by a heat rejection parameter β,

$$\beta = \frac{q}{f Q_f}. \tag{6}$$

The model accounts for hybrid electric propulsion systems by considering that the total electric load of the aircraft is contributed by the combination of power exported from the propulsion unit(s) w_x and the electrical power output from the batteries, w_b. The contribution from the batteries is characterized by battery parameter

$$\delta = \frac{w_b}{w_b + w_x}. \tag{7}$$

A negative value of the battery parameter signifies that the propulsion unit charges the battery, $\delta = 1$ indicates that all electrical load is met by the battery, and $\delta > 1$ indicates that the propulsion system receives supplementary power from the battery. Use of the battery does not itself contribute to contrail formation as no water vapor is emitted.

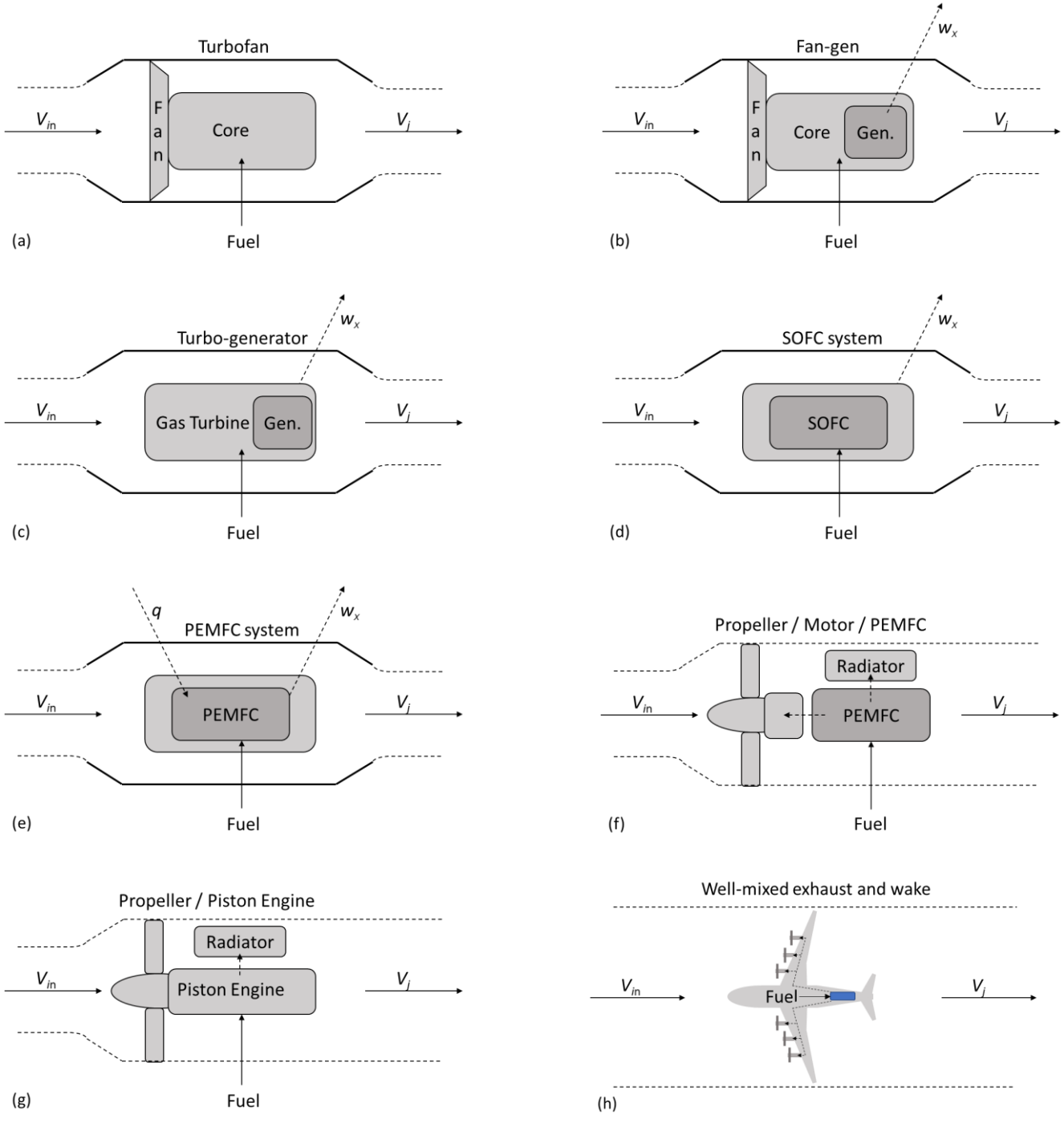

Fig. 3 Schematic illustration of propulsion architectures (a) turbofan, (b) fan-gen, (c) turbo-gen, (d) SOFC, (e) PEM Fuel Cell with external cooling, (f) PEM fuel cell with internal cooling within propeller wash, (g) piston engine-propeller system with cooling within the propeller wash, (h) distributed propulsion with well-mixed exhaust.

The generalized propulsion unit illustrated in Fig. 2 and characterized by parameters α, β, γ_i, γ_j, δ, η_x, η_{tr} and η_f can be used as a basis for evaluating the exhaust compositions and enthalpies for a wide range of propulsion technologies and configurations, of which several examples are illustrated highly schematically in Fig. 3. When analyzing the contrail propensity of a particular propulsion system precise values for these parameter may be known. Here, in order to make an overall illustrative comparison between different types of propulsion system, indicative parameter values are suggested for major types of propulsion system as discussed below and summarized in Table 1. A wide range of values might be applicable for any given parameter and plausible ranges are indicated in the following discussion. However to succinctly illustrate the ability of the new contrail formation model to provide a consistent means of comparison across many types of propulsion system, it has been necessary to present results for a single set of values for each propulsion system. The results thereby illustrate a number of significant differences and trends within/between propulsion system types, but the results should not be interpreted as an absolute quantitative prediction or ranking for any specific aircraft.

1. Gas turbine propulsion

Fig. 3a shows a model for a pure turbofan propulsion unit, where the core and bypass streams are assumed to be well-mixed within a short distance downstream of the engine, whereupon the fully-expanded exhaust is modeled with a uniform velocity V_j. For advanced high-bypass ratio turbofan engines, typically the jet velocity parameter is $\gamma_j \approx 0.85$ (range 0.8-0.9), transfer efficiency is effectively a turbomachinery isentropic efficiency $\eta_{tr} \approx 0.9$ (range $0.85 - 0.95$), and fuel efficiency is $\eta_f \approx 0.45$ [27] (range $0.35 - 0.5$ across numerous aeroengines) The engine shown does not export any work ($\alpha = 0$) nor does it employ external cooling ($\beta = 0$) – any blade cooling is achieved using fluids entirely within the propulsion unit.

In practice aircraft engines are required also to export power to auxiliary systems, increasingly in the form of electrical power [24]. Additionally, turbo-electric propulsion concepts are under development in which gas turbine engines export electrical power to drive separate electrically-powered fans or propellers [28]. The required electrical power may be produced by generators within the turbofan engine (see Fig. 3b), as for example in the STARC-ABL concept aircraft where two wing-mounted turbofan/generator ('fan-gen') units power a tail-mounted electric fan with power export factor $\alpha \approx 0.3$ [29], or by dedicated gas turbine generators (turbo-generators or auxiliary power units (APUs)) (see Fig. 3c) which make relatively little or no direct contribution to jet propulsion, $\alpha \approx 1$ [28]. The full range of possible power export factors is thereby encompassed by the three gas turbine examples evaluated here.

2. *Fuel cell propulsion*

Fig. 3d-f illustrate how the exhaust model may be applied to three examples of fuel cell propulsion systems. PEM fuel cells are restricted to low temperature operation, requiring cooling to maintain the membrane temperature typically to less than 100 °C, or to around 200 °C in so-called 'high temperature' systems [21]. If the cooling system rejects heat externally (Fig. 3e) then the heat release parameter can be determined to match the desired fuel cell operating temperature, typically $\beta \approx 0.4$ (range 0.3-0.45 for PEMFC) is required, depending on the cell efficiency and flight conditions. In contrast, solid oxide fuel cells operate only at elevated temperatures, supporting operation at higher pressure and potentially without cooling ($\beta = 0$, Fig. 3e) [20]. Due to their high-temperature capability, SOFC may be used in tandem with a gas turbine cycle to increase overall efficiency. In either case, if the cooling system rejects heat exclusively into the fluid comprising the humid exhaust stream (Fig. 3f) then there is no external heat exchange and $\beta = 0$. The fuel efficiency of proposed aeronautical fuel cell systems is around $\eta_f \approx 50\%$ (range 45-60%) for PEMFC and $\approx 60\%$ (range 50-70%) for SOFC, after accounting for the balance of plant [18].

Fuel cells may be integrated into an isolated single propulsion unit ($\alpha = 0$), perhaps containing a propeller (Fig. 3f), or used wholly or in part to supply external electrical loads and other electrical propulsion devices ($\alpha > 0$). In a pure fuel cell generator unit ($\alpha \approx 1$), the momentum of the flow through the fuel cell makes a very limited contribution to the thrust, and the fuel-air ratio or the equivalence ratio are more pertinent parameters to characterize operation, and from which it is possible to derive α. The equivalence ratio equals the ratio of the fuel-air ratio to the stoichiometric fuel-air ratio, $\phi = f/f_{st}$, such that values less than unity indicate the presence of excess air. PEMFC typically operate slightly fuel-lean, Gierens' analysis of fuel cell contrails assumes stoichiometric operation. This study assumes that fuel cells operate slightly lean at $\phi \approx 0.95$, noting that a wider range might be used in practice, $\phi \sim$ 0.7-1. Since there is little thrust provided by the flow through the fuel cell, a wide range of values could be considered for inlet velocity ($\gamma_i \in [0,1]$) and jet velocity parameter ($\gamma_j \in [0.8,2]$) dependent on the fuel cell installation, with little impact on contrail propensity.

3. *Piston engine propulsion*

Fig. 3g shows a model for a propulsion unit comprising a piston engine, radiator and propeller. It is assumed that the engine exhaust, the cooling flow through the radiator, and the flow through the propeller mix into a single exhaust stream with an effective velocity V_j. In the configuration shown, all of the engine's power is provided to the propeller and no power is exported from the unit ($\alpha = 0$). All of the cooling occurs within the propulsive stream and there is no external heat transfer ($\beta = 0$). The shaft fuel efficiency of aeronautical piston engines at cruise is typically $\eta_f \approx 40\%$ (range 25-45%) [30, 31].

4. *Propeller propulsion*

The generalized model requires a value for the overall fuel-air ratio of the combined propulsion stream. To apply the generalized model to combined propulsive streams including propeller wash, the air mass flow rate is approximated as $\dot{m}_a =$

$\rho A V_\infty$ where ρ is the ambient density, and A the propeller swept area. Assuming the effective net thrust of the propulsion stream $F_{N,eff}$ (i.e. net thrust after subtraction of any drag associated with the propulsion system installation [27]) and propeller efficiency η_p (the ratio of propulsive work to shaft work input, typically $\eta_p \approx 0.85$ (range 0.8-0.95)) are known, the effective fuel-air ratio, jet velocity and transfer efficiency are modeled for the propeller unit as,

$$f = \frac{1}{\eta_p \eta_f Q_f} \frac{F_{N,eff}}{\rho A}, \tag{8}$$

$$V_j = V_\infty + \frac{F_{N,eff}}{\rho A V_\infty}, \tag{9}$$

and

$$\eta_{tr} = \frac{\eta_p}{\gamma_j}. \tag{10}$$

5. *Boundary layer ingestion*

Boundary layer ingestion (BLI) is an approach where low-momentum fluid from the fuselage or wing boundary layers or wakes are fed into the propulsors, offering a reduction in drag and/or an increase in propulsive efficiency [32]. The effect of BLI on contrail propensity is taken into account in the model through the inflow velocity parameter γ_i, which is equal to unity for a propulsor mounted in the freestream, for example on a pylon below the wing. In the case of BLI the inflow velocity parameter depends on the relative thickness of the boundary layer versus the height of the intake scoop of the propulsion unit. To give an indicative value, we estimate that the inlet velocity parameter for the tail cone-mounted BLI fan of the STARC-ABL concept aircraft would be around 0.8 (based on intake areas quoted in Ref. [29]). However values approaching zero may arise if the propulsion unit draws air through, or from very near to the aerodynamic surfaces of the aircraft. To determine the enthalpy of the ingested fluid, it is assumed that the boundary layer decelerates the flow adiabatically and at constant static pressure.

6. *Mixing between multiple jets and wakes*

For future propulsion architectures where mixing occurs between exhaust from more than one type of propulsion unit, contrail assessment potentially may require more detailed analysis of multi-stream mixing and consideration of a multi-dimensional mixing manifold rather than the mixing curve considered in this work. However it may be expected that many relevant multi-stream distributed architectures can be approximated reasonably well using the binary mixing approach

presented herein if the propulsive streams become well mixed with one another prior to significant condensation taking place, as is the case for the core/bypass in most turbofan engines.

To illustrate the general effect of adopting more distributed propulsion architectures, results are presented for the limiting case where all propulsive streams and aircraft wakes become perfectly mixed, resulting in a single 'well-mixed' stream as illustrated in Fig. 3h. In this limit the momentum flux added to the propulsive streams exactly balances the momentum deficit of the airframe wakes in the direction of flight so that, neglecting the addition of fuel mass, $V_j = V_{in} = V_\infty$. Since all work and heat transfers occur within the aircraft system, $\alpha = 0$ and $\beta = 0$.

Table 1. Indicative exhaust model parameter values for various propulsion system configurations.

Configuration	Power export parameter	Heat rejection parameter	Inlet velocity parameter	Jet velocity parameter	Fuel efficiency	Transfer efficiency	Mech/Elec efficiency
	α	β	γ_i	γ_j	η_f	η_{tr}	η_x
Turbofan	0	0	1	0.85	45%	90%	-
Fan-gen	0.3	0	1	0.85	45%	90%	90%
Turbo-gen/APU	1	0	1	0.85	45%	90%	90%
SOFC	$\phi = 0.95$	0	1	2.0	60%	-	-
PEMFC	$\phi = 0.95$	~0.4[†]	1	2.0	55%	-	-
PEM/Prop	0	0	1	0.95	55%	90%	-
Piston/Prop	0	0	1	0.95	40%	90%	-
Well-mixed	0	0	1	1	45%	90%	-

7. Exhaust properties

Computation of the mixing curve requires the value of the specific stagnation enthalpy $h_{0,j}$ of the exhaust stream, as defined in the frame of reference moving with the atmosphere. The specific stagnation enthalpy combines the chemical and thermal energy (i.e. static enthalpy) with the kinetic energy of the flow. The stagnation enthalpy is used as it is necessary to account for conversion of kinetic energy into thermal energy as the exhaust mixes and decelerates towards the speed of the atmosphere.

First, the static enthalpy h_j of the exhaust stream is derived by considering the energy budget in the flows of air and fuel (subscripts a and f) that combine in the propulsion system to produce the exhaust stream (subscript j). Energy conservation

[†] The value of β is adjusted to maintain a PEM cell outlet stagnation temperature of 80°C.

in the steady-flow through the propulsion system is expressed in the form of the Steady-Flow Energy Equation: Velocities V_{in}, $V_{f,in}$ (the fuel inflow velocity), and V_j are measured in the frame of reference moving with the aircraft,

$$q - w_x = \left(h_a^{\ominus} - h_{a,in} - \frac{1}{2}V_{in}^2\right) + f\left(h_f^{\ominus} - h_{f,in} - \frac{1}{2}V_{f,in}^2\right) - fQ_f + (1+f)\left(h_j + \frac{1}{2}V_j^2 - h_j^{\ominus}\right). \tag{11}$$

The change in chemical energy between reactants (fuel and air) and products (exhaust gas) at reference conditions (e.g. 298.15 K), denoted by superscript $\ominus$, is taken into account by the term involving the lower calorific value,

$$fQ_f = h_a^{\ominus} + fh_f^{\ominus} - (1+f)h_j^{\ominus}. \tag{12}$$

The static enthalpy of the jet fluid is then found by rearrangement,

$$h_j = \frac{1}{1+f}\left[q - w_x + h_{a,in} + \frac{1}{2}V_{in}^2 - h_a^{\ominus} + f\left(h_{f,in} + \frac{1}{2}V_f^2 - h_f^{\ominus}\right) + fQ_f\right] + h_j^{\ominus} - \frac{1}{2}V_j^2. \tag{13}$$

Second, the stagnation enthalpy of the propulsive jet is found by adding its kinetic energy in the frame of reference of the atmosphere, $\frac{1}{2}(V_j - V_\infty)^2$. Recalling the definitions of β and η_f, the jet stagnation enthalpy is

$$h_{0j} = \frac{1}{1+f}\left[fQ_f(1-\beta-\eta_f') + h_{a,in} + f\left(h_{f,in} + \frac{1}{2}V_f^2\right)\right] + \frac{1}{2}(V_j - V_\infty)^2 + \left[h_j^{\ominus} - \frac{1}{1+f}h_a^{\ominus} - \frac{f}{1+f}h_f^{\ominus}\right], \tag{14}$$

where η_f' is an overall fuel efficiency introduced here to characterise the full range of propulsion units with ($\alpha > 0$) and without ($\alpha = 0$) export of power in a general way,

$$\eta_f' = (\alpha\eta_x + (1-\alpha)\eta_{tr})\eta_f. \tag{15}$$

The composition of the exhaust stream is evaluated considering overall chemical reaction of a fuel $C_aH_bO_cN_d$ with humid air with overall equivalence ratio ϕ. Neglecting other minor species in air and products, consideration of atomic conservation yields,

$$C_aH_bO_cN_d + \frac{x}{\phi}(O_2 + yN_2 + zH_2O) \rightarrow aCO_2 + \left(\frac{b}{2} + \frac{xz}{\phi}\right)H_2O + \left(\frac{x}{\phi} - a - \frac{b}{4} + \frac{c}{2}\right)O_2 + \left(\frac{d}{2} + \frac{xy}{\phi}\right)N_2 \quad (16)$$

where $x = a + b/4 - c/2$ is the number of moles of O_2 required for stoichiometric reaction, the molar ratio of nitrogen to oxygen in dry air is $y = 79/21$, and the molar ratio of water and oxygen atoms in the humid atmospheric air is

$$z = \frac{1 + y}{p_\infty/(\psi_l p_l^*) - 1}, \quad (17)$$

where ψ_l is the relative humidity with respect to the liquid water saturation pressure p_l^*. It follows that the equivalence ratio is related to the fuel air ratio by

$$\phi = f\frac{x\left(w_{O2} + yw_{N2} + zw_{H_2O}\right)}{w_{fuel}}, \quad (18)$$

with molar mass denoted by w. The mass fraction of water in the atmosphere and jet are then:

$$Y_{H_2O,\infty} = \frac{zw_{H_2O}}{w_{O_2} + yw_{N_2} + zw_{H_2O}}, \quad (19)$$

$$Y_{H_2O,j} = \frac{\left(\frac{b}{2} + \frac{xz}{\phi}\right)w_{H_2O}}{aw_{CO_2} + \left(\frac{b}{2} + \frac{xz}{\phi}\right)w_{H_2O} + \left(\frac{x}{\phi} - a - \frac{b}{4} + \frac{c}{2}\right)w_{O_2} + \left(\frac{d}{2} + \frac{xy}{\phi}\right)w_{N_2}}. \quad (20)$$

B. The mixing curve

The mixing curve describes the composition and thermodynamic states that arise as the humid exhaust stream mixes with ambient fluid. The present analysis is formulated in terms of mixture fraction, rather than the dilution factor used in traditional formulations [10], to provide a rigorous derivation starting from conservation of mass and energy where every additional

assumption is stated explicitly. The mixture fraction is used widely as a reference variable in turbulent reacting flow modeling [33] and is defined here as the local mass fraction of the fluid that originated from the humid exhaust stream.

Assuming that there is no preferential transport of mass due to non-unity molecular or turbulent Schmidt numbers, or due to slippage of any condensed-phase water relative to the gaseous mixture, conservation of mass and energy dictates that mixing between the exhaust stream and the atmosphere will yield a linear variation of stagnation enthalpy and mass fraction with respect to mixture fraction, ξ.

$$h_{0,mix} = (1-\xi)h_{0,\infty} + \xi h_{0,j}. \tag{21}$$

$$\boldsymbol{Y}_{mix} = (1-\xi)\boldsymbol{Y}_{\infty} + \xi \boldsymbol{Y}_{j}. \tag{22}$$

where subscripts mix, ∞, and j refer to the mixture, atmosphere and jet respectively, h_0 is the stagnation enthalpy in the frame of reference moving with the atmosphere, and $\boldsymbol{Y}$ is the vector of mass fractions of the N species in the mixture. This approach naturally accounts for any water mass ingested by the engine from the atmosphere [19].

Assuming that the humid exhaust velocity is uniform and fully-expanded at its effective point of release, and if the molecular and turbulent Schmidt numbers are unity, conservation of momentum dictates that the mean axial velocity of the mixture also follows a linear profile with respect to mixture fraction. V_{mix} is the mixture velocity defined in the frame of reference moving with the atmosphere,

$$V_{mix} = \xi\left(V_j - V_{\infty}\right). \tag{23}$$

The static enthalpy is obtained by subtracting the kinetic energy (in the frame of reference of the atmosphere) from the stagnation enthalpy,

$$h_{mix} = (1-\xi)h_{0,\infty} + \xi h_{0,j} - \frac{1}{2}\xi^2\left(V_j - V_{\infty}\right)^2. \tag{24}$$

The present formulation of the mixing curve in terms of mixture fraction differs from previous analyzes (e.g. Ref. [18]) that start from an assumption that mixing follows a straight line in H_2O partial pressure–temperature space. Since heat capacity and molar mass also depend on mixture fraction, it is clear that partial pressure cannot follow a straight line with respect to

temperature during mixing. The present formulation strictly enforces conservation of energy, mass and momentum (subject to the assumptions stated), and provides a rigorous means to evaluate the mixing curve without invoking perfect gas assumptions, and to assess the errors incurred by alternative formulations.

C. Contrail assessment

The onset of condensation is assessed by comparing the mixture partial pressure p_{H_2O} along the mixing curve to the saturation pressures of liquid water (p_l^*) and ice (p_s^*) at the mixture temperature. The saturation temperatures are modeled based on the Clausius-Clapeyron relation accounting for the variation of latent heat with temperature as in Bohren and Albrecht [34].

$$p_l^* = p_{ref}^* \left[(6808\ K) \left(\frac{1}{T_{ref}} - \frac{1}{T} \right) - 5.09 \ln \frac{T}{T_{ref}} \right], \tag{25}$$

$$p_s^* = p_{ref}^* \left[(6293\ K) \left(\frac{1}{T_{ref}} - \frac{1}{T} \right) - 0.555 \ln \frac{T}{T_{ref}} \right], \tag{26}$$

where $T_{ref} = 273\ K$ and $p_{ref}^* = 0.611\ kPa$.

The static pressure in the jet is assumed to be atmospheric. Therefore, prior to any condensation taking place, the partial pressure of water vapor in the mixture depends on the atmospheric pressure and the mixture mass fraction vector $\boldsymbol{Y}_{mix}$:

$$p_{H_2O} = p_{atm} \frac{\left(\frac{Y_{H_2O}}{W_{H_2O}} \right)}{\sum_{\alpha=1}^{N} \left(\frac{Y_\alpha}{W_\alpha} \right)}. \tag{27}$$

where subscript α refers to each of the N species in the mass fraction vector.

The corresponding mixture temperature is evaluated from the static enthalpy, Eq. (25), using a thermodynamic model f_T

$$T_{mix} = f_T(h_{mix}, p_\infty, \boldsymbol{Y}_{mix}) \tag{28}$$

Two thermodynamic models are used and compared in this study: the perfect gas model and a semi-perfect gas model for mixtures of water vapor, carbon dioxide, oxygen and nitrogen. The semi-perfect gas model uses the Shomate equation to evaluate species enthalpies as a function of temperature with coefficients from the Ref. [35]. Since water has a low partial

pressure throughout the mixing process and we are concerned initially with assessing the state prior to the onset of condensation, the semi-perfect gas model provides a highly accurate model for thermodynamic properties of exhaust-air mixtures.

Fuel thermodynamic properties are modeled using the REFPROP v. 10 software [36], using dodecane as a surrogate for kerosene, and using pure parahydrogen to model properties of hydrogen fuel. The lower calorific value at 25°C is taken as 43.0 MJ.kg^{-1} for kerosene and 120.0 MJ.kg^{-1} for hydrogen.

Given the formulation developed thus far, it is possible to determine the temperature and partial pressure along the gas-phase mixing curve (prior to any condensation), and to assess whether and where the mixing curve intersects with the saturation conditions, providing basic information about contrail propensity. For comparison with previous contrail assessments (e.g. [10, 18]) the gradient of the mixture H_2O partial pressure with respect to temperature, can be evaluated from the computed mixing curve. Since the mixing curve generally is not straight, and saturation conditions tend to occur near to the colder end of the mixing curve, the gradient evaluated at $\xi \to 0$ is reported and denoted as G_0.

D. Simplified perfect gas model

Employing a perfect gas model $h = c_p\left(T - T^{\ominus}\right)$ for gaseous species enthalpies in Eq. (15) gives,

$$T_{0j} = \frac{1}{1+f}\left[\frac{fQ_f}{c_p}\left(1-\beta-\eta_f'-\kappa_f\right)+T_{in}\right]+\frac{1}{2c_p}\left(V_j-V_\infty\right)^2+\frac{f}{1+f}T^{\ominus}, \tag{29}$$

Since fuel typically is stored as a liquid, the perfect gas model should not be applied to the inlet fuel state and $\kappa_f = \left(\hat{h}_f^{\ominus} - \hat{h}_{f,in} - V_f^2/2\right)/Q_f$ represents the enthalpy required to bring the fuel from its stored state into the gas phase at the reference temperature: $\kappa_f \approx 3.5\%$ for liquid hydrogen and $\kappa_f \approx 0.6\%$ for liquid kerosene fuel. The circumflex accent indicates that fuel enthalpies $\hat{h}_f^{\ominus}$ and $\hat{h}_{f,in}$ must be evaluated with a two-phase thermodynamic model, rather than the perfect gas model, and REFPROP v.10 [36] is used in this study.

Following the derivation of Eq. (25), the perfect gas model then gives the mixture temperature as,

$$T_{mix} = (1-\xi)T_\infty + \xi\left[\frac{1}{1+f}\left[\frac{fQ_f}{c_p}\left(1-\beta-\eta_f'-\kappa_f\right)+T_{in}+fT^{\ominus}\right]+\frac{1-\xi}{2c_p}\left(V_j-V_\infty\right)^2\right] \tag{30}$$

Given the assumption that the intake flow is adiabatic, the inlet temperature is

$$T_{in} = T_\infty + \frac{V_\infty^2}{2c_p}(1-\gamma_i^2). \tag{31}$$

Substituting for T_{in} and for $V_j = (2/\gamma_j - 1)V_\infty$ yields,

$$T_{mix} = T_\infty + \frac{f\xi}{1+f}\left(T^{\ominus} - T_\infty\right) + \xi\left[\frac{f}{1+f}\frac{Q_f}{c_p}\left(1-\beta-\eta_f'-\kappa_f\right) + \frac{V_\infty^2}{2c_p}\left(\frac{1-\gamma_i^2}{1+f} + 4(1-\xi)\left(\frac{1}{\gamma_j}-1\right)^2\right)\right]. \tag{32}$$

For fuel air ratio $f \ll 1$, the prefect gas model simplifies to,

$$T_{mix} \approx T_\infty + \xi\left[\frac{fQ_f}{c_p}\left(1-\beta-\eta_f'-\kappa_f\right) + \frac{V_\infty^2}{2c_p}\left\{(1-\gamma_i^2) + 4(1-\xi)\left(\frac{1}{\gamma_j}-1\right)^2\right\}\right]. \tag{33}$$

The water partial pressure of the mixture is

$$p_{H_2O} = p_{atm}\frac{\left(Y_{H_2O,\infty} + \xi f EI_{H_2O}/(1+f)\right)/w_{H_2O}}{\sum_{\alpha=1}^{N}(Y_\alpha/w_\alpha)}. \tag{34}$$

where w_α denotes species molar mass. Approximating the molar mass of the mixture as that of air, $\epsilon = w_{H_2O}/w_{air} = 0.622$, and given that $f \ll 1$,

$$p_{H_2O} \approx \psi_l p_l^* + \xi\frac{f p_{atm} EI_{H_2O}}{\epsilon}. \tag{35}$$

The gradient of partial pressure with respect to temperature then is given by taking the ratio of derivatives $dp_{H_2O}/d\xi$ and $dT_{mix}/d\xi$,

$$G_{PG} = \frac{c_p p_{atm}}{\epsilon}\frac{EI_{H2O}}{\left(1-\beta-\eta_f'-\kappa_f\right)Q_f + \frac{V_\infty^2}{2f}\left[(1-\gamma_i^2) + 4(1-2\xi)\left(\frac{1}{\gamma_j}-1\right)^2\right]}. \tag{36}$$

The various design and operating parameters of the generalized propulsion model appear explicitly in this single prefect gas formula, providing insight into their relative contributions to contrail propensity: increasing any of $\beta, \eta_f', \kappa_f, \gamma_i$, or EI_{H2O}/Q_f, or moving γ_j closer to unity, tends to increase G and hence the propensity for contrail formation. Notably, given its variation with mixture fraction, the gradient of the mixing curve is not in fact constant, even given the perfect gas approximation.

E. Consistency and validity

The generalized model developed above reduces to and is consistent with previous models for the contrail factor [10, 18] when subject to their approximations and assumptions. The generalized model therefore retains the validity of the Schmidt-Appleman theory as expressed in the previous widely accepted models, but also removes potential limitations of the perfect gas approximation and extends applicability to a wide variety of potential propulsion architectures. For example, it is shown in the Appendix that the generalized model is equivalent to the contrail factor for conventional piston or gas turbine engines as expressed in Eq. (1) when taking $\eta_o = \eta_f \eta_{tr} \gamma_j$, provided that $\alpha = 0$, $\beta = 0$, $\gamma_i = 1$, $\kappa_f = 0$, the mixture is treated as a perfect gas, fuel mass is neglected, and one considers the contrail factor at the atmospheric end of the mixing curve, i.e. $\xi \to 0$. The generalized model for G is also equivalent to Gierens' formulation for uncooled fuel cells [18] taking η_f to be the ratio of electrical energy output to fuel calorific value, provided that $\alpha = 1$, $\beta = 0$, $\gamma_i = 0$, $\gamma_j = 2$, $\eta_x = 1$, the mixture is treated as a perfect gas with specific heat capacity equal to the value in the exhaust gas (denoted $\overline{c_p}$ by Gierens), fuel mass is neglected, and one considers the gradient at the atmospheric end of the mixing curve, i.e. $\xi \to 0$. Gierens argues that the impact of the difference in heat capacity is small, however it appears that Gierens erroneously evaluated the heat capacity of the exhaust mixture at the ambient temperature, thereby significantly reducing the difference, and there remains a need for a rigorous assessment of the perfect gas approximation for fuel cell applications.

The following section assesses the impact of the traditional perfect gas modeling approximations, and then provides illustrative predictions to show the impact of prospective changes in fuel type and propulsion system architecture for contrail propensity of alternative future aircraft.

III. Results and Discussion

A. The perfect gas approximation

The effects of the perfect gas approximation, neglect of fuel mass flow ($f \sim 0$), and neglect of the fuel storage enthalpy (κ_f) are illustrated by the mixing curves shown in Fig. 4 for the case of a typical turbofan and for a solid oxide fuel cell propulsion system, both for kerosene and for liquid hydrogen fuels when flying at Mach 0.78 and 10,000 m altitude. These

results refer only to one specific flight condition, but the differences between models and propulsion architectures are indicative of those observed across all sub-sonic flight conditions.

Figure 4 shows only a low-temperature portion of the mixing curves close to the saturation curves, and the exhaust temperatures are substantially hotter for some propulsion systems. The exhaust static temperature of the turbofan engines is taken as the mixed-out value for the core and bypass streams, resulting in a static temperature of around -20°C due to dilution of the hot core exhaust by low temperature bypass air. The exhaust temperature of an uncooled SOFC is substantially greater and the full mixing curves predicted for the hydrogen SOFC shown in Fig. 5 extend up to between 824°C and 1266°C, depending on the thermodynamic modelling assumptions. At these elevated temperatures, the mixing curve predicted by the more accurate semi-perfect gas model shows significant non-linearity.

The perfect gas model is evaluated either with a specific heat capacity value of cold air (1005 $J.kg^{-1}.K^{-1}$) or, following Gierens [18], with the specific heat capacity $c_{p,prod}$ of the exhaust gas composition and temperature (here evaluated with the semi-perfect gas model). For the kerosene-fuelled turbofan (Fig. 4a) there is relatively little error caused by the various simplifications. The turbofan prediction errors increase when considering liquid hydrogen fuel: in particular, neglecting the liquid fuel storage enthalpy (setting $\kappa_f = 0$) increases the exhaust temperature significantly. The effect of the fuel enthalpy (κ_f) is more significant for the SOFC than the turbofan because the exhaust is less dilute. Generally, however, the error due to neglecting fuel mass is small.

Errors are markedly greater for the SOFC propulsion system, especially with liquid hydrogen fuel (Fig. 4d) since the higher water concentration and temperature produces greater variation in specific heat capacity along the mixing curve. Towards the high temperature end of the mixing curve the error shown in Fig. 5 due to the perfect gas approximation is as large as 400°C. The perfect gas model based on the exhaust heat capacity performs relatively well at higher temperature, however evaluation of the Schmidt-Appleman criterion depends more upon the accuracy of the low-temperature portion of the mixing curve. For this reason, if using a perfect gas model to assess the Schmidt-Appleman criterion, it is more appropriate to use the heat capacity of ambient air, rather than Gierens' proposal to use the heat capacity of the exhaust stream [18].

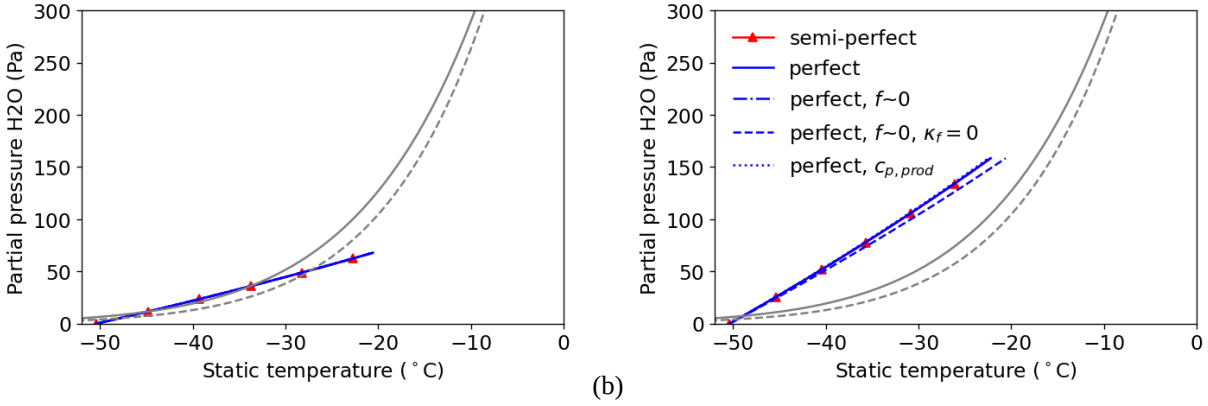

(a) (b)

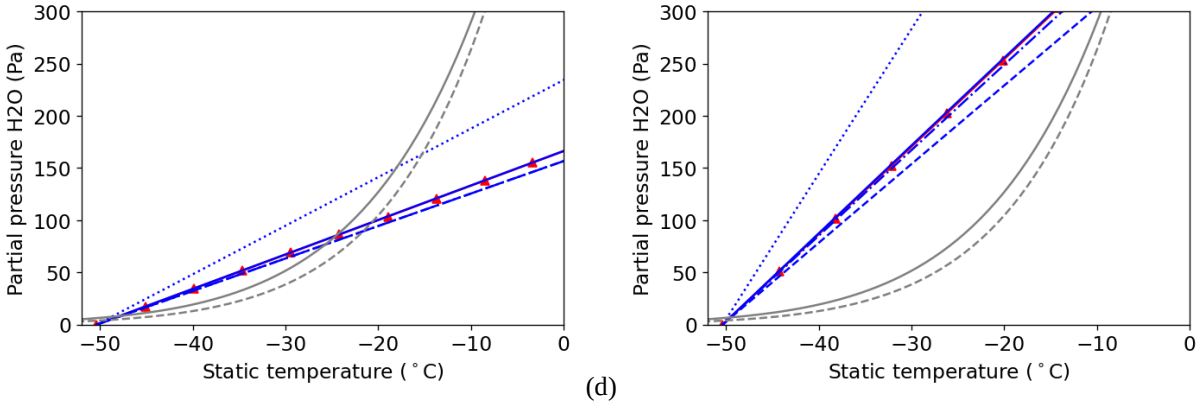

Fig. 4. Mixing curve predictions up to 0°C for various thermodynamic models: (a) kerosene turbofan, (b) hydrogen turbofan, (c) kerosene SOFC, (d) hydrogen SOFC. Saturation curves as in Fig. 1.

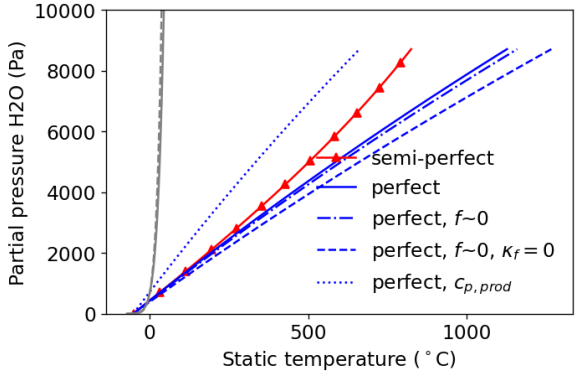

Fig. 5. Mixing curve predictions for various thermodynamic models applied to the hydrogen SOFC, showing the full temperature range. Saturation curves as in Fig. 1.

To quantify the practical impact of the perfect gas approximation, Table 2 presents predictions for G_0, T_{min}, T_{max} and for the contrail ceiling H_{min} determined numerically with the semi-perfect gas model, and using the conventional perfect gas model (Eq. 1) and the new generalized perfect gas model (Eq. 36). The contrail ceiling is the minimum altitude at which contrails form under saturated conditions in the International Standard Atmosphere – it gives a relative indication of the altitude below which different types of aircraft should fly to avert the possibility of generating contrails. H_{min} is evaluated by numerically determining the altitude at which the ambient temperature in the International Standard Atmosphere (ISA) is equal to T_{max} Note that additional criteria for whether such contrails would freeze and persist, and for the quantity of exhaust humidity that might freeze have not been employed here, and that contrail forming regions of the atmosphere in practice are highly localised.

Non-linearity of the mixing curve means that a numerical search must be performed to determine whether the mixing curve intersects with the saturation curves, and to find precise values of T_{min} and T_{max}. While such calculations each take

only a fraction of a second, even this computational overhead preferably would be avoided where contrail formation is to be assessed for very many different scenarios, for example as part of air traffic optimisation. Numerical iteration can be avoided by taking a linear approximation of the mixing curve based on a representative gradient $G \approx G_0$, with the initial gradient G_0 of the mixing curve determined numerically from the semi-perfect gas model, or algebraically with the approximations in Eqs. 1 or 36. Predictions for different propulsion architectures given by solution of the semi-perfect gas model (Semi-P), for the linearisation of the semi-perfect gas model (Linear) and for the perfect gas approximations in Eqs. 1 and 36 are presented in Table 2. Linearisation of the semi-perfect gas model results in error in T_{max} on the order of 2 K, and under-predictions of H_{min} by around 200-500 m depending on the fuel and the propulsion system. H_{min} is underpredicted predominantly because the heat capacity and kinetic energy increase along the mixing curve. The generalized perfect gas model predictions (Eq. 36) are very close to those of the linearized semi-perfect gas model, as may be expected. While errors in altitude of 500 m are unsatisfactory from the perspective of flight planning, these two linear models reproduce all of the trends predicted by the full semi-perfect gas model. and do provide a useful quantitative approximation to changes in T_{max} and H_{min} due to substantial changes between different types of propulsion architecture that change T_{max} and H_{min} by much more than 2 K and 500 m.

Given a value of G, direct determination of T_{max} from Eq. 25 requires numerical solution or, following Ref. [18], T_{max} can be approximated using the following curve fits

$$T_{max} = 226.69 + 9.43\ln(G - 0.053) + 0.720[\ln(G - 0.053)]^2 \quad for\ G \leq 2\ Pa/K \tag{37}$$

$$T_{max} = 226.031 + 10.2249\ln G + 0.335372(\ln G)^2 + 0.0642105(\ln G)^3 \quad for\ G > 2\ Pa/K \tag{38}$$

with T_{max} in K and G in Pa.K^{-1}. These curve fits give errors in T_{max} of less than 0.2 K compared to numerical solution of Eq. 25, and this error is acceptably small compared to the larger errors associated with approximating the mixing curve as a straight line or treating the mixture as a perfect gas. Evaluation of T_{min} is approximated by [18],

$$T_{min} \approx T_{max} - p_l^*(T_{max})/G. \tag{39}$$

The conventional perfect gas model (Eq. 1) is in close agreement with Eq. 36 for the case of kerosene-fuelled turbofan engines, but deviates significantly for hydrogen fuel and for other configurations embodying features that it does not take into account, such as the effects of increasingly distributed propulsion in the fan-gen and turbo-gen cases, effects of boundary

layer ingestion, or conversion to fuel cell propulsion. If a perfect gas model is required for these applications, the generalized model in Eq. 36 should be used in preference to Eq. 1. However to avoid unnecessary error, the semi-perfect gas model can be used in most applications with negligible computational overhead. The results shown in subsequent sections are computed using the semi-perfect gas model.

B. Alternative propulsion architectures

The effect of different types of propulsion technology on contrail propensity is illustrated by mixing curve predictions in Fig. 6 for the eight propulsion configurations set out in Fig. 3 and Table 1, both for kerosene and liquid hydrogen fuel, flying at Mach 0.78 and 10,000 m altitude. The gradients of the mixing curves are found to be insensitive to flight Mach number and ambient humidity. The contrail factor predicted using the perfect gas model is exactly independent of flight Mach number and the semi-perfect gas model gives an insignificant variation in contrail factor with flight Mach number (less than 0.1% between 0.4 and 0.78 flight Mach number) resulting from the variation of heat capacities along the mixing curve.

Gas turbine systems

Fig. 6a and b show predictions for three types of gas turbine propulsion systems with equal fuel efficiencies η_f. The main difference between the turbofan, fan-gen and turbo-gen mixing predictions is the exhaust temperature (-22.2°C, -10.2°C, 474.8°C respectively in the case of hydrogen fuel). A similar amount of enthalpy is extracted from the core flow in each case, but in the case of turbofan and fan-gen engines the core flow is diluted by the bypass stream before emission, so that the mixing curve does not extend as far. Since the turbofan and fan-gen engines mix the core exhaust with the bypass before discharge, and the bypass stream has higher enthalpy than ambient air, the turbofan and fan-gen exhausts have more heat per unit humidity than the turbo-gen engine and correspondingly have lower contrail factors. For all cases the contrail factor is around 2.5 times greater for hydrogen fuel on account of the greater hydrogen content per unit of calorific value. The absolute predictions are sensitive to the assumed fuel efficiency of the underlying gas turbine, but for gas turbines with similar level of technology and hence fuel efficiency, this analysis provides a robust illustration of the trend towards more electric aircraft.

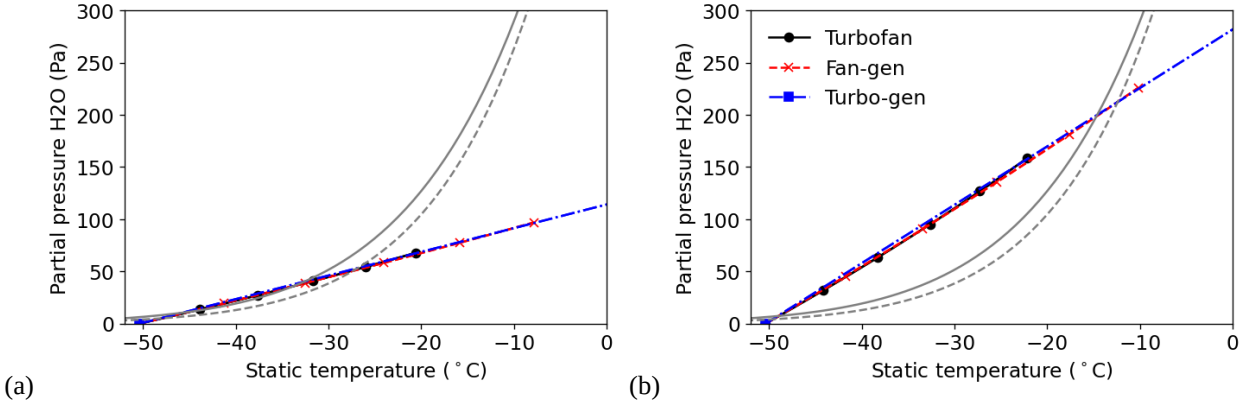

(a) (b)

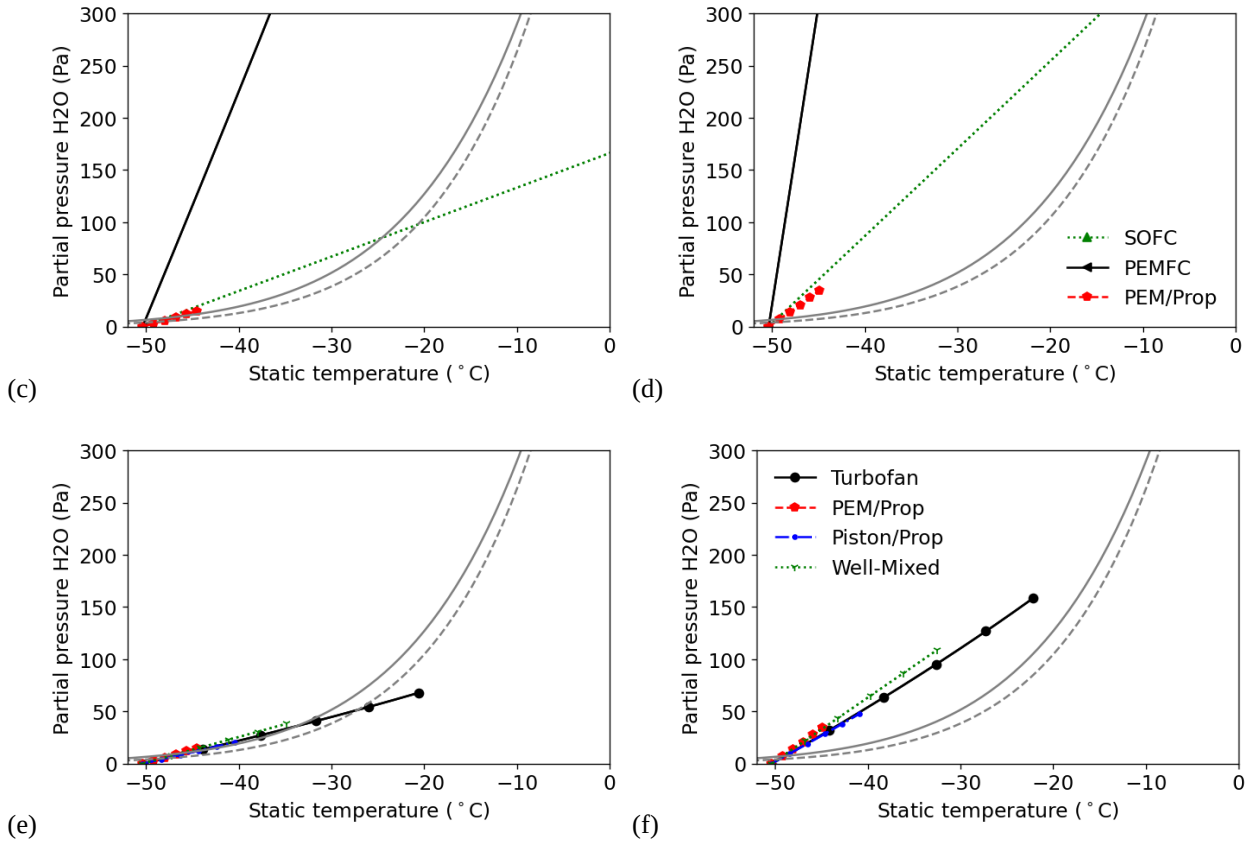

Fig. 6 Mixing curve predictions for alternative propulsion architectures with kerosene (left) and liquid hydrogen (right). Comparison of turbofan, fan-gen, and turbo-gen (a,b); SOFC, PEMFC, and PEM/Propeller (c,d); Turbofan, PEM/Propeller, Piston/Propeller, and Well-Mixed limit (e,f).

Fuel cell systems

Fig. 6c and d show predictions for three types of fuel cell propulsion system for kerosene and for liquid hydrogen fuels. For hydrogen fuel, the externally-cooled PEM fuel cell type has a markedly greater contrail factor compared to the uncooled SOFC on account of its reduced exhaust temperature (80°C versus 824°C). The internally-cooled PEM fuel cell (PEM/Propeller) incorporates the warmed coolant flow into the humid exhaust giving a contrail factor similar to the SOFC. The relative performance of the PEM/Propeller and SOFC systems is dependent on the assumed fuel efficiency and inlet/jet velocities, however the predictions robustly demonstrate the dramatic impact of external fuel cell cooling which greatly promotes condensation even at low altitude.

Propulsion architecture

Fig. 6e and f compare kerosene and hydrogen predictions across four general propulsion architectures – turbofan, PEM/Propeller, Piston engine/Propeller, and for the well-mixed limit of distributed-propulsion. The length of the mixing curve of the well-mixed system depends somewhat arbitrarily on the size of the stream tube that is assumed to contain the aircraft wakes and its propulsive jets, however the contrail factor for the well-mixed system is independent of the stream tube size. The gradients of the respective mixing curves reflect the relative overall efficiencies assumed for the different

architectures, and the ranking of these different types of propulsion system is sensitive to the performance of the specific technologies considered for each system.

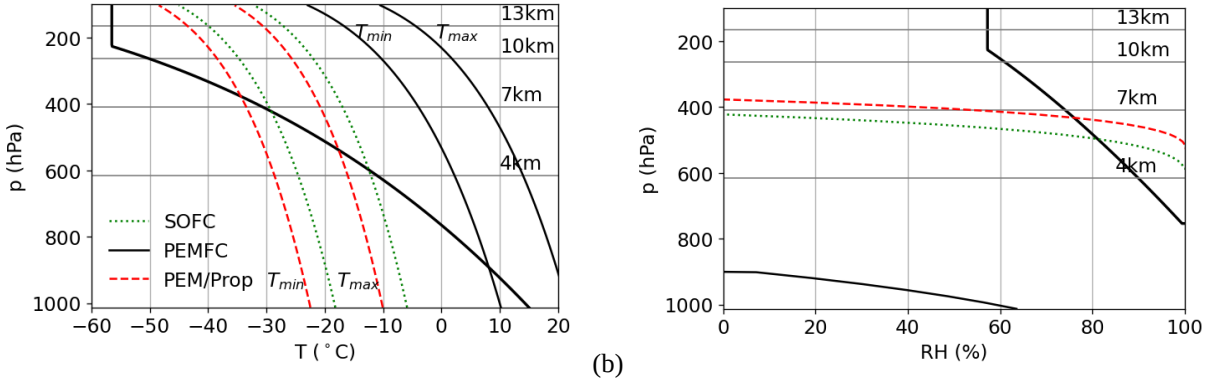

Fig. 7 Profiles of T_{min} and T_{max} (a) and relative humidity for contrail formation in ISA (b) for hydrogen-fueled fuel cell systems. Thick black temperature line represents the ISA, thick black relative humidity line represents ice saturation.

Atmospheric implications

Differences in propulsion architecture also affect the altitude, ambient temperature and relative humidity at which contrails form, as illustrated in Fig. 7 for hydrogen-fuelled fuel cell systems set out in Table 1. The figure illustrates T_{min}, T_{max}, and the relative humidity required for contrail formation in the ISA varying with altitude. The minimum altitude for contrail formation in a saturated environment is described as the contrail ceiling, H_{min}, corresponding to the 100% relative humidity end points of the curves Fig. 7b. In Fig. 7a contrails can or always form at altitudes where the T_{max} or T_{min} lines respectively are above the ambient temperature line (top right corner). In the relative humidity plot (Fig. 7b), contrails can form above a minimum altitude (maximum atmospheric pressure) plotted for each of the propulsion architectures. The greatest risk of persistent contrail cirrus arises where contrail formation occurs to the right of the ice saturation line, in the upper-right corner of Fig. 7b. The T_{min}, T_{max}, and relative humidity for the other propulsion architectures set out in Table 1 with hydrogen and kerosene fuels all follow similar profiles to those shown in Fig. 7 but with temperature profiles translated laterally and relative humidity profiles translated vertically. The effects of different propulsion system types are summarized by T_{min} and T_{max} values at 10 km altitude and by H_{min} values given in Table 2.

Table 2. Contrail factor, T_{min}, and T_{max} at 10 km altitude, and minimum altitude H_{min} for contrail formation in saturated International Standard Atmosphere estimated with the generalized semi-perfect gas model with numerical solution, with linearization, and with the new (Eq. 36) and conventional (Eq. 1) perfect gas models.

Config.	Model	Kerosene				Hydrogen			
		G_0 [Pa.K^{-1}]	T_{min} [°C]	T_{max} [°C]	H_{min} [km]	G_0 [Pa.K^{-1}]	T_{min} [°C]	T_{max} [°C]	H_{min} [km]
Turbofan	**Semi-P**	2.05	-49.8	-36.8	7.35	5.02	-40.4	-27.6	5.43
	Linear	2.05	-49.4	-39.6	7.84	5.02	-40.3	-29.5	5.63
	(Eq.36)	2.04	-49.4	-39.6	7.85	5.04	-40.2	-29.4	5.63
	(Eq.1)	2.07	-49.3	-39.5	7.82	4.84	-40.7	-29.9	5.74
Fan-gen	**Semi-P**	2.11	-49.5	-36.5	7.29	5.18	-40.1	-27.3	5.35
	Linear	2.11	-49.1	-39.3	7.77	5.18	-39.9	-29.1	5.55
	(Eq.36)	2.11	-49.1	-39.3	7.78	5.21	-39.9	-29.1	5.55
	(Eq.1)	2.07	-49.3	-39.5	7.82	4.84	-40.7	-29.9	5.74
Turbo-gen	**Semi-P**	2.26	-48.8	-35.8	7.15	5.58	-39.3	-26.5	5.18
	Linear	2.26	-48.4	-38.5	7.62	5.58	-39.1	-28.2	5.35
	(Eq.36)	2.26	-48.4	-38.5	7.62	5.61	-39.1	-28.2	5.34
	(Eq.1)	2.07	-49.3	-39.5	7.82	4.84	-40.7	-29.9	5.74
SOFC	**Semi-P**	3.29	-45.0	-32.1	6.37	8.36	-34.8	-22.1	4.22
	Linear	3.29	-44.7	-34.4	6.72	8.36	-34.7	-23.3	4.20
	(Eq.36)	3.30	-44.6	-34.3	6.71	8.45	-34.6	-23.1	4.18
	(Eq.1)								
PEMFC	**Semi-P**	21.45	-23.6	-11.2	1.75	56.92	-10.4	1.7	0.00
	Linear	21.45	-23.5	-10.8	1.09	56.92	-10.4	3.9	0.00
	(Eq.36)	22.72	-22.7	-10.0	0.87	63.58	-8.9	5.7	0.00
	(Eq.1)								
PEM /Prop.	**Semi-P**	2.42	-48.1	-35.1	7.01	5.98	-38.5	-25.7	5.02
	Linear	2.42	-47.8	-37.8	7.46	5.98	-38.4	-27.4	5.15
	(Eq.36)	2.42	-47.8	-37.8	7.46	6.02	-38.3	-27.3	5.15
	(Eq.1)	2.44	-47.7	-37.7	7.44	5.71	-38.9	-28.0	5.30
Piston/ Prop.	**Semi-P**	1.99	-50.1	-37.1	7.41	4.88	-40.7	-27.9	5.49
	Linear	1.99	-49.6	-39.9	7.90	4.88	-40.6	-29.8	5.71
	(Eq.36)	1.99	-49.7	-39.9	7.91	4.90	-40.5	-29.8	5.71
	(Eq.1)	2.00	-49.6	-39.8	7.90	4.69	-41.0	-30.3	5.82
Well-mixed	**Semi-P**	2.46	-48.0	-35.0	6.98	6.09	-38.3	-25.5	4.98
	Linear	2.46	-47.6	-37.6	7.42	6.09	-38.2	-27.2	5.10
	(Eq.36)	2.46	-47.6	-37.6	7.42	6.13	-38.1	-27.1	5.10
	(Eq.1)	2.28	-48.4	-38.4	7.60	5.33	-39.6	-28.8	5.48
Turbofan-BLI	**Semi-P**	1.60	-52.2	-39.2	7.84	3.90	-43.2	-30.3	6.00
	Linear	1.60	-51.7	-42.2	8.39	3.90	-42.9	-32.4	6.29
	(Eq.36)	1.60	-51.7	-42.2	8.39	3.90	-42.9	-32.4	6.30
	(Eq.1)	2.17	-48.8	-39.0	7.71	5.09	-40.1	-29.3	5.61

The most significant factor affecting atmospheric conditions for contrail formation is the fuel type. For example, the various kerosene-fuelled combustion engines only produce contrails above 7.0-7.9 km in the standard atmosphere, and these minimum altitudes reduce by around 2 km when switching to liquid hydrogen fuel.

More-electric aircraft and distributed propulsion

There is a comparatively smaller difference in contrail factor between the various gas turbine propulsion systems. However increasing electrification of the aircraft power/propulsion systems still leads to a substantial reduction in the contrail ceiling, with transition from conventional turbofan engines to pure turbo-gen engines reducing H_{min} by around 200 m. The

trend towards distributed propulsion also reduces the contrail ceiling, by around 400 m in the limit of perfectly well-mixed exhaust/wakes due to the high overall efficiency.

Fuel cell cooling

The contrail ceiling also reduces by around 1.2 km as a result of the improved overall efficiencies assumed for hydrogen fuel cell systems compared to conventional turbofan engines. The additional effect of external cooling used in the PEMFC system is very dramatic, bringing the contrail ceiling close to sea level. This highlights the importance of accounting for fuel cell cooling, an aspect absent in previous analysis of fuel cell contrail emission [18]. Despite the propensity for fuel cell aircraft exhaust to condense, their impact on radiative forcing may be less significant due to anticipated operation of such aircraft at relatively low altitudes where fine ice particles are less likely to form and persist [18].

Boundary layer ingestion

The effect of boundary layer ingestion is assessed by considering a turbofan propulsion system with inflow velocity parameter $\gamma_i = 0.8$. To enable a fair and practically-relevant comparison, the engine specific thrust is kept unchanged (i.e. 82.4 m.s^{-1} at Mach 0.78, 10 km altitude) by increasing the jet velocity parameter from 0.85 to 0.929. This is a highly simplified representation of the effects of boundary layer ingestion on a turbofan aircraft neglecting, for example, possible effects on engine efficiency and effects on the downwash interactions between wing tip vortices and the propulsive jets. With this caveat in mind, the model predicts a 22% reduction in contrail factor, and 480 m and 470 m increases in the contrail ceiling for kerosene and hydrogen respectively. The analysis shows that boundary layer ingestion tends to reduce contrail propensity for two reasons: first the static temperature of the air entering the engine is greater due to the viscous heating in the boundary layer upstream of the engine; second, in the frame of reference of the atmosphere, kinetic energy contributes a smaller percentage of the exhaust stagnation enthalpy resulting in a hotter exhaust for a given specific thrust. The author is not aware of previous studies setting out the significant potential of boundary layer ingestion to reduce contrail propensity. Given also the potential efficiency benefit of boundary layer ingestion, it is proposed that boundary layer ingestion should be investigated further as a practical means to reduce contrail emission.

IV.Conclusions

The Schmidt-Appleman theory for contrail formation has been applied rigorously without use of the perfect gas assumption. Conventional use of the perfect gas approximation, neglect of fuel mass, and neglect of the sensible and latent heat of liquid fuels (especially liquid hydrogen) results in significant errors that are easily avoided with the semi-perfect gas formulation provided here. An updated perfect gas formulation is also provided, demonstrating consistency with previous analyzes, and taking account explicitly of the key properties of alternative propulsion systems that affect contrail propensity. A generalized model for the exhaust temperature and composition of a wide range of alternative propulsion architectures is presented and applied systematically to gas turbine, piston engine, and fuel cell systems with kerosene and hydrogen fuel,

also accounting for effects of fuel cell cooling, distributed propulsion, and boundary layer ingestion. Use of the perfect gas approximation tends to increase the altitude at which contrails are predicted to form by 200-500 m, depending on the propulsion system and fuel, and use of the semi-perfect gas approach presented here is recommended for improved accuracy.

The generalized model provides the means to conduct consistent comparisons of contrail propensity between different types of propulsion system, and confirms trends predicted previously using separate models derived for different kinds of propulsion system: Transition to hydrogen fuel has a very dramatic effect on contrail formation, reducing the altitude ceiling at which exhaust can condense by around 2 km. The trend towards more efficient propulsion systems also increases contrail propensity, both due to increased efficiencies of fuel cells or more advanced combustion engines, and due to increased propulsive efficiency enabled by, for example, distributed electric propulsion. The trend towards more-electric aircraft also is shown to reduce the contrail ceiling, by up to around 400 m because more energy is removed from the humid exhaust flow and distributed around the aircraft. The new formulation accounts for cooling required by low-temperature (e.g. PEM) fuel cells, showing that cooling the exhaust to 80°C leads to exhaust condensation at less than 2km above sea level. The analysis shows that, while many the propulsion system developments under consideration for reducing CO_2 emission promote contrail formation, boundary layer ingestion might be used to reduce contrail propensity and to extend the altitude range in which aircraft can operate without generating contrails, warranting more detailed investigation of this possibility.

Appendix: Consistency with Schmidt-Appleman formula

The generalized model in Eq. (36) applied to a perfect gas and neglecting fuel mass, taking $\alpha = 0, \beta = 0, \gamma_i = 1, \kappa_f = 0, \eta_o = \gamma_j \eta_f \eta_{tr}$, gives the contrail factor

$$G = \frac{c_p p_{atm}}{\epsilon} \frac{EI_{H2O}}{(1-\eta'_f)Q_f + \frac{2V_\infty^2}{f}\left(\frac{1}{\gamma_j} - 1\right)^2} \tag{40}$$

Consistency with the Schmidt-Appleman formula (Eq. 1) requires

$$(1-\eta_f\eta_{tr})Q_f + \frac{2V_\infty^2}{f}\left(\frac{1}{\gamma_j} - 1\right)^2 = (1-\eta_f\eta_{tr}\gamma_j)Q_f, \tag{41}$$

which simplifies algebraically to the requirement:

$$fQ_f\eta_f\eta_{tr}\gamma_j = 2V_\infty^2\left(\frac{1}{\gamma_j} - 1\right). \tag{42}$$

For a system operating with $V_{in} = V_\infty$ and neglecting fuel mass flow, the definitions of η_f and η_{tr} gives

$$fQ_f\eta_f\eta_{tr}\gamma_j = \frac{\gamma_j}{2}\left(V_j^2 - V_\infty^2\right). \tag{43}$$

Using the definition of the jet velocity parameter, $V_j = V_\infty(2/\gamma_j - 1)$,

$$fQ_f\eta_f\eta_{tr}\gamma_j = \frac{\gamma_j}{2}V_\infty^2\left(\left(\frac{2}{\gamma_j} - 1\right)^2 - 1\right), \tag{44}$$

which simplifies to

$$fQ_f\eta_f\eta_{tr}\gamma_j = 2V_\infty^2\left(\frac{1}{\gamma_j} - 1\right), \blacksquare \tag{45}$$

thereby demonstrating consistency between the generalized model (Eq. 36) and the traditional Schmidt-Appleman formulation (Eq. 1).

Acknowledgements

I am grateful to the anonymous reviewers who proposed many improvements to this work. This work has received financial support from the UK Natural Environment Research Council grant number NE/Z503824/1.

References

[1] Brewer, A. W., "Condensation Trails," *Weather*, Vol. 1, No. 2, 1946, pp. 34–40. https://doi.org/10.1002/j.1477-8696.1946.tb00024.x

[2] Appleman, H., "The Formation of Exhaust Condensation Trails by Jet Aircraft," *Bulletin of the American Meteorological Society*, Vol. 34, No. 1, 1953, pp. 14–20. https://doi.org/10.1175/1520-0477-34.1.14

[3] Lee, D. S., Fahey, D. W., Skowron, A., Allen, M. R., Burkhardt, U., Chen, Q., Doherty, S. J., Freeman, S., Forster, P. M., and Fuglestvedt, J., "The Contribution of Global Aviation to Anthropogenic Climate Forcing for 2000 to 2018," *Atmospheric Environment*, Vol. 244, 2021, Paper 117834. https://doi.org/10.1016/j.atmosenv.2020.117834http://dx.doi.org/10.1016/j.atmosenv.2020.117834

[4] Williams, V., Noland, R., and Toumi, R., "Air Transport Cruise Altitude Restrictions to Minimize Contrail Formation," *Climate Policy*, Vol. 3, No. 3, 2003, pp. 207–219. https://doi.org/10.3763/cpol.2003.0328

[5] Noppel, F., and Singh, R., "Overview on Contrail and Cirrus Cloud Avoidance Technology," *Journal of Aircraft*, Vol. 44, No. 5, 2007, pp. 1721–1726. https://doi.org/10.2514/1.28655

[6] Gierens, K., Lim, L., and Eleftheratos, K., "A Review of Various Strategies for ContrailAvoidance," *Open Atmospheric Science Journal*, Vol. 2, No. 1, Jan. 2008, pp. 1–7. https://doi.org/10.2174/1874282300802010001

[7] Haglind, F., "Potential of Lowering the Contrail Formation of Aircraft Exhausts by Engine Re-Design," *Aerospace Science and Technology*, Vol. 12, No. 6, 2008, p. 490–497. https://doi.org/10.1016/j.ast.2007.12.001

[8] Burkhardt, U., Bock, L., and Bier, A., "Mitigating the Contrail Cirrus Climate Impact by Reducing Aircraft Soot Number Emissions," *NPJ Climate Atmosphseric Science*, Vol. 1, No. 37, 2018, pp. 1–7. https://doi.org/10.1038/s41612-018-0046-4

[9] Schmidt, E., "Die Entstehung von Eisnebel aus den Auspuffgasen von Flugmotoren," *Schriften der Deutschen Akademie der Luftfahrtforschung*, Vol. 44, No. 5, 1941, pp. 1–15.

[10] Schumann, U., "On Conditions for Contrail Formation from Aircraft Exhausts," *Meteorologische Zeitschrift*, Vol. 5, No. 1, 1996, pp. 4–23. https://doi.org/10.1127/metz/5/1996/4

[11] Wall, E., "Material zur Frage der Eiskeimbildung in der Atmosphäre," *Meteorologische Zeitschrift*, Vol. 59, No. 4, 1942, pp. 109–120.

[12] Weickmann, H., "Formen und Bildung Atmosphaerischer Eiskristalle," *Beiträge Zur Physik der Atmosphäre*, Vol. 28, 1945, pp. 12–52.

[13] Murphy, D., and Koop, T., "Review of the Vapour Pressures of Ice and Supercooled Water for Atmospheric Applications," *Quarterly Journal of the RoyalMeteorological Society*,Vol. 131,No. 608, 2005, pp. 1539–1565. https://doi.org/10.1256/qj.04.94

[14] Pruppacher, H., and Klett, J., *Microphysics of Clouds and Precipitation*, Reidel Publishing, Dordrecht, The Netherlands, 1997.

[15] Irvine, E., Hoskins, B., and Shine, K., "A Lagrangian Analysis of Ice-Supersaturated Air over the North Atlantic," *Journal of Geophysical Research Atmospheres*, Vol. 119, No. 1, 2013, pp. 90–100. https://doi.org/10.1002/2013JD020251

[16] Bier, A., Unterstrasser, S., Zink, J., Hillenbrand, D., Jurkat-Witschas, T., and Lottermoser, A., "Contrail Formation on Ambient Aerosol Particles for Aircraft with Hydrogen Combustion: A Box Model Trajectory Study," *Atmospheric Chemistry and Physics*, Vol. 24, No. 4, 2024, pp. 2,319–2344. https://doi.org/10.5194/acp-24-2319-2024

[17] Ström, L., and Gierens, K., "First Simulations of Cryoplane Contrails," *Journal of Geophysical Research: Atmospheres*, Vol. 107, No. D18, 2002, p. 4346. https://doi.org/10.1029/2001JD000838

[18] Gierens, K., "Theory of Contrail Formation for Fuel Cells," *Aerospace*, Vol. 8, No. 164, 2021, pp. 1–13. https://doi.org/10.3390/aerospace8060164

[19] Verma, P., and Burkhardt, U., "Contrail Formation Within Cirrus: ICON-LEM Simulations of the Impact of Cirrus Cloud Properties on Contrail Formation," *Atmospheric Chemistry and Physics*, Vol. 22, No. 13, 2022, pp. 8819–8842. https://doi.org/10.5194/acp-22-8819-2022

[20] Fernandes, M. D., Andrade, S. D. P., Bistritzki, V. N., Fonseca, R. M., Zacarias, L. G., Gonçalves, H. N. C., de Castro, A. F., Domingues, R. Z., and Matencio, T., "SOFC-APU Systems for Aircraft: A Review," *International Journal of Hydrogen Energy*, Vol. 43, No. 33, 2018, pp. 16,311–16,333. https://doi.org/10.1016/j.ijhydene.2018.07.004

[21] Wang, Y., Diaz, D. F. R., Chen, K. S., Wang, Z., and Adroher, X. C., "Materials, Technological Status, and Fundamentals of PEM Fuel Cells – A Review," *Materials Today*, Vol. 32, Jan. 2020, pp. 178–203. https://doi.org/10.1016/j.mattod.2019.06.005

[22] Yin, F., Grewe, V., and Gierens, K., "Impact of Hybrid-Electric Aircraft on Contrail Coverage," *Aerospace*, Vol. 7, No. 10, 2020, p. 147. https://doi.org/10.3390/aerospace7100147

[23] Kim, H. D., Perry, A. T., and Ansell, P. J., "A Review of Distributed Electric Propulsion Concepts for Air Vehicle Technology," *AIAA/IEEE Electric Aircraft Technologies Symposium (EATS)*, AIAA Paper 2018-4998, 2018. https://doi.org/10.2514/6.2018-4998

[24] Madonna,V., Giangrande, P., and Galea,M., "Electrical Power Generation in Aircraft:Review, Challenges, and Opportunities," *IEEE Transactions on Transportation Electrification*, Vol. 4, No. 3, 2018, pp. 646–659. https://doi.org/10.1109/TTE.2018.2834142

[25] Kim, H. D., Brown, G. V., and Felder, J. L., "Distributed Turboelectric Propulsion for HybridWing Body Aircraft," *International Powered Lift Conference, Royal Aeronautical Soc.*, 2008.

[26] Miller, R. J., "Mechanical Work Potential," *Proceedings of the ASME Turbo Expo 2013: Turbine Technical Conference and Exposition*, Vol. 6A: Turbomachinery, New York, June 2013, p. V06AT36A032. https://doi.org/10.1115/GT2013-95488

[27] Cumpsty, N., and Heyes, A., *Jet Propulsion*, 3rd ed., Cambridge Univ. Press, Cambridge, England, U.K., 2015.

[28] Alrashed, M., Nikolaidis, T., Pilidis, P., and Jafari, S., "Utilisation of Turboelectric Distribution Propulsion in Commercial Aviation: A Review on NASA's TeDP Concept," *Chinese Journal of Aeronautics*, Vol. 34, No. 11, 2021, pp. 48–65. https://doi.org/10.1016/j.cja.2021.03.014

[29] Welstead, J., and Felder, J. L., "Conceptual Design of a Single-Aisle Turboelectric Commercial Transport with Fuselage Boundary Layer Ingestion," *54th AIAA Aerospace Sciences Meeting*, AIAA Paper 2016-1027, Jan. 2016. https://doi.org/10.2514/6.2016-1027

[30] Altuntas, O., "Comparing Different Piston-Prop Aircraft Angines with Combustion Efficiency and Exergy," *Journal of Thermal Analysis Calorimetry*, Vol. 145, June 2021, pp. 659–667. https://doi.org/10.1007/s10973-020-09926-y

[31] Piancastelli, L., and Francia, D., "Recent Improvements in Piston Engine Performance for a New Generation of Aircraft Propulsion Systems," *Atti del XIX Congresso nazionaleAIDAA*, Rome, 2007, pp. 113–124.

[32] Hendricks, E. S., "A Review of Boundary Layer Ingestion Modeling Approaches for Use in Conceptual Design," NASATM-219926, 2018.

[33] Peters, N., *Turbulent Combustion*, Cambridge Univ. Press, Cambridge, England, U.K., 2000.

[34] Bohren, C., and Albrecht, B., *Atmospheric Thermodynamics*, Oxford Univ. Press, New York, 1998.

[35] Chase, M. W., Jr., "NIST-JANAF Themochemical Tables, 4th ed.," Journal of Physical Chemistry Reference Data, Monograph, Vol. 9, New York, 1998, pp. 1–1951.

[36] Lemmon, E. W., Bell, I. H., Huber, M. L., and McLinden, M. O., *NIST Standard Reference Database 23: Reference Fluid Thermodynamic and Transport Properties-REFPROP*, Version 10.0, National Inst. of Standards and Technology, Standard Reference Data Program, Gaithersburg, MD, 2018. https://doi.org/10.18434/T4/1502528

[1] Brewer, A. W., “Condensation Trails,” Weather, Vol. 1, No. 2, 1946, pp. 34–40.
https://doi.org/10.1002/j.1477-8696.1946.tb00024.x

[2] Appleman, H., “The Formation of Exhaust Condensation Trails by Jet Aircraft,” Bulletin of the American Meteorological Society, Vol. 34, No. 1, 1953, pp. 14–20.
https://doi.org/10.1175/1520-0477-34.1.14

[3] Lee, D. S., Fahey, D. W., Skowron, A., Allen, M. R., Burkhardt, U., Chen, Q., Doherty, S. J., Freeman, S., Forster, P. M., and Fuglestvedt, J., “The Contribution of Global Aviation to Anthropogenic Climate Forcing for 2000 to 2018,” Atmospheric Environment, Vol. 244, 2021, Paper 117834.
https://doi.org/10.1016/j.atmosenv.2020.117834http://dx.doi.org/10.1016/j.atmosenv.2020.117834

[4] Williams, V., Noland, R., and Toumi, R., “Air Transport Cruise Altitude Restrictions to Minimize Contrail Formation,” Climate Policy, Vol. 3, No. 3, 2003, pp. 207–219.
https://doi.org/10.3763/cpol.2003.0328

[5] Noppel, F., and Singh, R., “Overview on Contrail and Cirrus Cloud Avoidance Technology,” Journal of Aircraft, Vol. 44, No. 5, 2007, pp. 1721–1726.
https://doi.org/10.2514/1.28655

[6] Gierens, K., Lim, L., and Eleftheratos, K., “A Review of Various Strategies for ContrailAvoidance,” Open Atmospheric Science Journal, Vol. 2, No. 1, Jan. 2008, pp. 1–7.
https://doi.org/10.2174/1874282300802010001

[7] Haglind, F., “Potential of Lowering the Contrail Formation of Aircraft Exhausts by Engine Re-Design,” Aerospace Science and Technology, Vol. 12, No. 6, 2008, p. 490–497.
https://doi.org/10.1016/j.ast.2007.12.001

[8] Burkhardt, U., Bock, L., and Bier, A., “Mitigating the Contrail Cirrus Climate Impact by Reducing Aircraft Soot Number Emissions,” NPJ Climate Atmosphseric Science, Vol. 1, No. 37, 2018, pp. 1–7.
https://doi.org/10.1038/s41612-018-0046-4

[9] Schmidt, E., “Die Entstehung von Eisnebel aus den Auspuffgasen von Flugmotoren,” Schriften der Deutschen Akademie der Luftfahrtforschung, Vol. 44, No. 5, 1941, pp. 1–15.

[10] Schumann, U., “On Conditions for Contrail Formation from Aircraft Exhausts,” Meteorologische Zeitschrift, Vol. 5, No. 1, 1996, pp. 4–23.
https://doi.org/10.1127/metz/5/1996/4

[11] Wall, E., “Material zur Frage der Eiskeimbildung in der Atmosphäre,” Meteorologische Zeitschrift, Vol. 59, No. 4, 1942, pp. 109–120.

[12] Weickmann, H., “Formen und Bildung Atmosphaerischer Eiskristalle,” Beiträge Zur Physik der Atmosphäre, Vol. 28, 1945, pp. 12–52.

[13] Murphy, D., and Koop, T., “Review of the Vapour Pressures of Ice and Supercooled Water for Atmospheric Applications,” Quarterly Journal of the RoyalMeteorological Society,Vol. 131,No. 608, 2005, pp. 1539–1565.
https://doi.org/10.1256/qj.04.94

[14] Pruppacher, H., and Klett, J., Microphysics of Clouds and Precipitation, Reidel Publishing, Dordrecht, The Netherlands, 1997.

[15] Irvine, E., Hoskins, B., and Shine, K., “A Lagrangian Analysis of Ice-Supersaturated Air over the North Atlantic,” Journal of Geophysical Research Atmospheres, Vol. 119, No. 1, 2013, pp. 90–100.
https://doi.org/10.1002/2013JD020251

[16] Bier, A., Unterstrasser, S., Zink, J., Hillenbrand, D., Jurkat-Witschas, T., and Lottermoser, A., “Contrail Formation on Ambient Aerosol Particles for Aircraft with Hydrogen Combustion: A Box Model Trajectory Study,” Atmospheric Chemistry and Physics, Vol. 24, No. 4, 2024, pp. 2,319–2344.
https://doi.org/10.5194/acp-24-2319-2024

[17] Ström, L., and Gierens, K., "First Simulations of Cryoplane Contrails," Journal of Geophysical Research: Atmospheres, Vol. 107, No. D18, 2002, p. 4346.
https://doi.org/10.1029/2001JD000838

[18] Gierens, K., "Theory of Contrail Formation for Fuel Cells," Aerospace, Vol. 8, No. 164, 2021, pp. 1–13.
https://doi.org/10.3390/aerospace8060164

[19] Verma, P., and Burkhardt, U., "Contrail Formation Within Cirrus: ICON-LEM Simulations of the Impact of Cirrus Cloud Properties on Contrail Formation," Atmospheric Chemistry and Physics, Vol. 22, No. 13, 2022, pp. 8819–8842.
https://doi.org/10.5194/acp-22-8819-2022

[20] Fernandes, M. D., Andrade, S. D. P., Bistritzki, V. N., Fonseca, R. M., Zacarias, L. G., Gonçalves, H. N. C., de Castro, A. F., Domingues, R. Z., and Matencio, T., "SOFC-APU Systems for Aircraft: A Review," International Journal of Hydrogen Energy, Vol. 43, No. 33, 2018, pp. 16,311–16,333.
https://doi.org/10.1016/j.ijhydene.2018.07.004

[21] Wang, Y., Diaz, D. F. R., Chen, K. S., Wang, Z., and Adroher, X. C., "Materials, Technological Status, and Fundamentals of PEM Fuel Cells – A Review," Materials Today, Vol. 32, Jan. 2020, pp. 178–203.
https://doi.org/10.1016/j.mattod.2019.06.005

[22] Yin, F., Grewe, V., and Gierens, K., "Impact of Hybrid-Electric Aircraft on Contrail Coverage," Aerospace, Vol. 7, No. 10, 2020, p. 147.
https://doi.org/10.3390/aerospace7100147

[23] Kim, H. D., Perry, A. T., and Ansell, P. J., "A Review of Distributed Electric Propulsion Concepts for Air Vehicle Technology," AIAA/IEEE Electric Aircraft Technologies Symposium (EATS), AIAA Paper 2018-4998, 2018.
https://doi.org/10.2514/6.2018-4998

[24] Madonna,V., Giangrande, P., and Galea,M., "Electrical Power Generation in Aircraft:Review, Challenges, and Opportunities," IEEE Transactions on Transportation Electrification, Vol. 4, No. 3, 2018, pp. 646–659.
https://doi.org/10.1109/TTE.2018.2834142

[25] Kim, H. D., Brown, G. V., and Felder, J. L., "Distributed Turboelectric Propulsion for HybridWing Body Aircraft," International Powered Lift Conference, Royal Aeronautical Soc., 2008.

[26] Miller, R. J., "Mechanical Work Potential," Proceedings of the ASME Turbo Expo 2013: Turbine Technical Conference and Exposition, Vol. 6A: Turbomachinery, New York, June 2013, p. V06AT36A032.
https://doi.org/10.1115/GT2013-95488

[27] Cumpsty, N., and Heyes, A., Jet Propulsion, 3rd ed., Cambridge Univ. Press, Cambridge, England, U.K., 2015.

[28] Alrashed, M., Nikolaidis, T., Pilidis, P., and Jafari, S., "Utilisation of Turboelectric Distribution Propulsion in Commercial Aviation: A Review on NASA's TeDP Concept," Chinese Journal of Aeronautics, Vol. 34, No. 11, 2021, pp. 48–65.
https://doi.org/10.1016/j.cja.2021.03.014

[29] Welstead, J., and Felder, J. L., "Conceptual Design of a Single-Aisle Turboelectric Commercial Transport with Fuselage Boundary Layer Ingestion," 54th AIAA Aerospace Sciences Meeting, AIAA Paper 2016-1027, Jan. 2016.
https://doi.org/10.2514/6.2016-1027

[30] Altuntas, O., "Comparing Different Piston-Prop Aircraft Angines with Combustion Efficiency and Exergy," Journal of Thermal Analysis Calorimetry, Vol. 145, June 2021, pp. 659–667.
https://doi.org/10.1007/s10973-020-09926-y

[31] Piancastelli, L., and Francia, D., "Recent Improvements in Piston Engine Performance for a New Generation of Aircraft Propulsion Systems," Atti del XIX Congresso nazionaleAIDAA, Rome, 2007, pp. 113–124.

[32] Hendricks, E. S., "A Review of Boundary Layer Ingestion Modeling Approaches for Use in Conceptual Design," NASATM-219926, 2018.

[33] Peters, N., Turbulent Combustion, Cambridge Univ. Press, Cambridge, England, U.K., 2000.

[34] Bohren, C., and Albrecht, B., Atmospheric Thermodynamics, Oxford Univ. Press, New York, 1998.

[35] Chase, M. W., Jr., "NIST-JANAF Themochemical Tables, 4th ed.," Journal of Physical Chemistry Reference Data, Monograph, Vol. 9, New York, 1998, pp. 1–1951.

[36] Lemmon, E. W., Bell, I. H., Huber, M. L., and McLinden, M. O., NIST Standard Reference Database 23: Reference Fluid Thermodynamic and Transport Properties-REFPROP, Version 10.0, National Inst. of Standards and Technology, Standard Reference Data Program, Gaithersburg, MD, 2018.
https://doi.org/10.18434/T4/1502528